Effect of rapid solidification on the synthesis and thermoelectric properties of Yb-filled Co4Sb12 skutterudite

Effect of rapid solidification on the synthesis and thermoelectric properties of Yb-filled Co_4Sb_{12} skutterudite

F. Aversano[1], S. Branz[1], E. Bassani[2], C. Fanciulli[2], A. Ferrario[3], S. Boldrini[3], M. Baricco[1,*], A. Castellero[1]

[1]University of Turin, Department of Chemistry & NIS Centre, Turin, Italy

[2]CNR – ICMATE, Lecco Unit, Lecco, Italy

[3]CNR – ICMATE, Padova Unit, Padova, Italy

[*]corresponding author (M. Baricco). E-mail address: marcello.baricco@unito.it; tel.: +39 0116707569; fax: +39 0116707855

Abstract

In this work the effect of different processing routes on the kinetics of formation of Co_4Sb_{12} phase and Yb filling in the skutterudite cage, as well as thermoelectric behaviour was evaluated.

As prepared slowly cooled ingot and rapidly solidified ribbons show the presence of multiple phases, as a consequence of the complex solidification path characterized by two peritectic reactions. As solidification rate increases, grain refinement is promoted. Annealing of rapidly solidified ribbons induces a faster solubilisation of Yb due to increased grain boundary diffusivity. For this reason, rapid solidification can be considered a promising intermediate step for lowering the total processing time of skutterudites.

Sintering of powders obtained from the slowly cooled ingot and rapidly solidified ribbons leads to the formation of massive samples with different densities, depending on the particle size distributions of the starting powders. The effect of Yb content on the thermoelectric properties was critically analysed, considering both data from the literature and this work.

Keywords: thermoelectricity; skutterudite; phonon scattering; rapid solidification; diffusion.

Introduction

The interest in thermoelectric materials raises from their ability to convert wasted heat into electricity in reliable and long standing solid state devices, improving energy efficiency. The thermoelectric performance of materials is characterized by the dimensionless figure of merit $ZT = \frac{S^2\sigma}{\kappa}T$, where S is the Seebeck coefficient, σ is the electrical conductivity, T is the absolute temperature and κ is the total thermal conductivity, containing electronic, lattice and bipolar contributions ($\kappa = \kappa_{el} + \kappa_{lat} + \kappa_{bp}$). The ideal thermoelectric material should have a high power factor, $PF = S^2\sigma$, and low thermal conductivity in a wide range of temperature. However, the interdependence of S, σ and κ_{el} leads to an intrinsic maximum limit of ZT in correspondence of a certain charge carrier concentration [1]. ZT can be further improved by reducing the lattice thermal conductivity since it can be decoupled from the electronic contribution without varying the charge carrier concentration [1].

Filled skutterudites can have high electrical conductivity like a crystal and low thermal conductivity like a glass, which make them excellent thermoelectric material according to the phonon glass electron crystal (PGEC) concept [2]. In fact, the presence of two large interstices inside the elementary cell allows to insert interstitial atoms such as lanthanides [3,4] or alkaline earth metals [5,6], acting as phonon scattering centres without affecting electrical conductivity. The filler content is ruled by electronic issues [7-11]. Skutterudites based on the elements of the group 9 (Co, Rh, Ir) and pnictogen elements (P, As, Sb) are electronically stable and can be only partially filled according to the valence state of the filler ion. In the case of Co_4Sb_{12}, Yb is one of the ideal filler species, due to its heavy mass and small radius compared to others. Conversely to trivalent lanthanide ions, Yb allows to optimize electronic properties as a consequence of the mixed valence state (Yb^{2+} and Yb^{3+}) [3, 9]. It was shown that the contribution of Yb^{2+} ion increases with the Yb occupancy factor in the cell [11], allowing the extension of the solubility range of the filler. The effect of the filler amount in $Yb_xCo_4Sb_{12}$ on the thermoelectric properties was studied by several authors [12-24]. The solubility of Yb in the skutterudite cell depends on the synthesis process [13],

the temperature and the Co/Sb ratio [19].The actual amount of Yb in the cell is usually lower than the nominal one [9, 16], due to its volatility and tendency to form oxides, affecting thermoelectric performance. The desired amount of Yb in the compound can be attained by adding an excess of Yb (30-50 mol.%) [9, 16].

A step forward for the commercial exploitation of skutterudites in thermoelectric applications is to establish a reliable, reproducible and affordable processing route. Skutterudites processed directly from the melt are affected by solidification segregation, originating from the peritectic reactions in the binary phase diagram (see for instance Ref. [25] for Co-Sb), that induces porosity, chemical inhomogeneity, secondary phase formation, incomplete filling of the skutterudite cell, and, consequently, poor thermoelectric performances [13, 22]. Possible solutions to this problem are 1) performing a solid/liquid reaction between $CoSb_2$ and Sb [22], 2) stirring the liquid before casting [13], 3) cooling following an oscillating temperature gradient [26], 4) direct formation of the skutterudite phase by deep undercooling of the liquid through rapid solidification techniques [27]. Rapid solidification allows to obtain refined microstructures [28] and, in some cases, even amorphous phases [29]. The introduction of a high density of interfaces in grain refined materials leads to a reduction of the lattice thermal conductivity with respect to coarse microstructures obtained by conventional processing routes [30].

Scope of this work is to employ rapid solidification as an intermediate step in the processing of Yb-filled Co_4Sb_{12} and to evaluate its effect on the kinetics of single phase formation and Yb filling. The effect of the Yb filling on thermoelectric properties is critically discussed in the frame of a literature survey.

Experimental

Elemental Co (rod, 99.995 %), Sb (shots, 99.999 %) and Yb (powder, 99.9 %) were weighed according to the nominal stoichiometry ($Yb_{0.25}Co_4Sb_{12}$) and placed into graphite coated quartz ampoules. The ampoules were sealed under vacuum (10^{-5} mbar) and placed in a muffle furnace for the following heat treatment: 1) slow heating (6 hours) from room temperature to 1473 K, 2) isotherm at 1473 K for 5 h (the ampoule was shacked every hour to guarantee homogenization of

the melt), 3) free cooling in the furnace to room temperature. In this way, ingots of the master alloy were obtained.

Rapid solidification of the alloy was performed using a planar flow casting apparatus (Edmund Bühler GmbH), where the master alloy ingot was induction melted in a BN crucible under Ar atmosphere and the melt was injected under a pressure of 0.2 bar onto a copper wheel rotating at 20 m/s, forming ribbons 20-30 μm thick. The cooling rate during rapid solidification is estimated to be 10^5 K/s [28].

Phase evolution in master alloy ingots (bulk) and rapidly solidified samples (RS) was studied by isothermal annealing at 898 K for 1, 2, 4 days.

Powders for sintering were obtained by hand grinding in an agate mortar the following precursors:

- Master alloy ingots annealed for 4 days at 898 K (powder 1);
- rapidly solidified ribbons annealed for 4 days at 898 K (powder 2);
- as quenched rapidly solidified ribbons without annealing (powder 3).

Finally, powders 1, 2 and 3 were sintered by Open Die Pressing (ODP) [31] obtaining samples ODP1, ODP2 and ODP3, respectively. The powders were loaded in Fe sheath, preheated at 823 K for 10 min before sintering between two heated plates at 748 K for 10 min applying a load of 200 MPa. At the end of the sintering procedure, load was released and heating of the plates was switched off. In the case of samples ODP1 and ODP2, the samples were slowly cooled between the plates passing from 748 K to 373 K into 2 hours, while in the case of ODP3 the sample was subjected to free cooling, covering the same temperature gap in 30 min.

Structural characterization was carried out by X-ray diffraction (XRD) using a Panalytical X'Pert instrument with Cu Kα radiation (λ = 1.5406 Å) working at 40 kV and 30 mA. The values of lattice parameter and Yb occupancy factor at 2a site in the skutterudite cage were refined by Rietveld method using the software MAUD [32]. The microstructure and chemical composition were monitored by Scanning Electron Microscopy (SEM) using a Zeiss EVO 50 XVP – LaB_6 equipped with an Oxford Instruments INCA Energy 250 Energy Dispersive X-ray analyzer (EDX).

Thermoelectric properties of the sintered samples were measured as a function of temperature. ODP 2 was measured up to 873 K, while ODP3 was measured up to 688 K (below the sintering

temperature) in order to avoid the annealing of the sample and preserve the microstructure obtained after sintering. Seebeck coefficient, S, and electrical conductivity, σ, were measured by means of a custom built apparatus [33] applying a heating ramp of 2 K/min and working under helium flow (200 sccm/min) . The thermal conductivity (κ) was calculated according to the formula $\kappa = \alpha\rho C_p$, where α is the thermal diffusivity, ρ is the mass density and C_p is the specific heat capacity. The thermal diffusivity (α) of 10 mm x 10 mm samples was measured by the laser flash method (LFA 457 MicroFlash, Netzsch, Selb, Germany) under Ar flow. The mass density (ρ) was evaluated by Archimedes' principle with a pycnometer and specific heat capacity (C_p) was determined by differential scanning calorimetry, DSC (Perkin Elmer DSC 7), according to the following procedure. Heating ramps at 10 K/min were performed in a temperature range of 30 K. Each ramp was preceded and followed by a long isotherm in order to stabilize the signal. The measurement was repeated with the empty alumina pans, a standard (zaffire) and the sample. The specific heat of the sample, C_p^s, at different temperatures was obtained by comparing the signals measured for the sample and the standard using the “height method” and the “area method” through the relationships [34]

$$C_p^s = C_p^z \frac{(\Delta Y_s - \Delta Y_0)}{(\Delta Y_z - \Delta Y_0)} \frac{m_z}{m_s} \quad (1)$$

where C_p^z is the specific heat of the standard, ΔY_s and ΔY_z are the calorimetric signals of the sample and the standard, respectively, ΔY_0 is the calorimetric signal of the empty pans, m_z and m_s are the mass of the standard and the sample, respectively, and

$$C_p^s = C_p^z \frac{(\Delta H_s - \Delta H_0)}{(\Delta H_z - \Delta H_0)} \frac{m_z}{m_s} \quad (2)$$

where C_p^z is the specific heat of the standard, ΔH_s and ΔH_z are the integrated areas under the calorimetric signals of the sample and the standard, respectively, ΔH_0 is the integrated area under the calorimetric signal of the empty pans, m_z and m_s are the mass of the standard and the sample, respectively. Measurements were performed on ODP2 and ODP3 samples and the values of specific heat obtained for the two samples with the two methods were averaged at each temperature.

Results and discussion

EDX analysis of all the samples revealed a ratio Sb/Co slightly larger than the stoichiometry (3:1), as reported in table 1 and table 2, indicating that equilibrium is attained in the two phases region $CoSb_3$ + Sb [19], where the solubility of Yb in the skutterudite depends on the Sb/Co ratio. Even if close to the detection limit of the technique, the total amount of Yb measured by EDX (1.0-1.2 at.%) is lower than the expected equilibrium value (1.5 at.%), indicating that a fraction of the Yb powder was not successfully alloyed and confirming the difficulty to maintain the Yb stoichiometry in the alloy, as already highlighted in Ref. [9] and Ref. [16].

The XRD pattern of the as prepared master alloy ingot (bulk), Figure 1(a), shows only the crystallographic reflections of the $CoSb_3$ phase. However, backscattered electrons SEM micrographs of the same sample (not shown) reveal the presence of additional phases ($CoSb_2$, CoSb, $YbSb_2$) dispersed in the $CoSb_3$ matrix, indicating that the alloy did not reach the equilibrium because of the slow kinetics of the peritectic reactions

$$CoSb + \text{liquid} \rightarrow CoSb_2 \quad (3)$$

$$CoSb_2 + \text{liquid} \rightarrow CoSb_3 \quad (4).$$

After annealing at 898 K for 4 days, the XRD pattern of the bulk shows only the crystallographic reflections of the $CoSb_3$ phase, Figure 1(b). Again, backscattered electrons SEM micrographs of the annealed bulk, Figure 2(a), show the presence of the same additional phases ($CoSb_2$, CoSb, $YbSb_2$) observed in the corresponding as prepared sample, indicating that the alloy did not reach the equilibrium, even after annealing at high temperature.

In the case of the as quenched ribbon, the XRD pattern, Figure 1(c), reveals the presence of five phases ($CoSb_3$, $CoSb_2$, CoSb, $YbSb_2$ and Sb) indicating that the system is out of the equilibrium, as a consequence of the high cooling rate experienced by the alloy during rapid solidification. Figure 2(c) shows the SEM micrograph of the longitudinal cross section of the ribbon, obtained with the backscattered electrons detector. The lower edge of the ribbon is smooth while the upper edge is rough, indicating that the former solidified in contact with the copper substrate (wheel side) and the latter solidified in contact with the argon atmosphere (free side). The micrograph is characterized by different levels of grey, indicating the presence of several phases, in agreement

with the XRD pattern, Figure 1(c). The microstructure becomes progressively coarser from the wheel side to the free side, because of the progressive reduction of the cooling rate from the wheel to the free side.

After annealing the ribbon at 898 K for 4 days, the formation of a single phase is promoted, as shown by the XRD pattern, Figure 1(d), and by the backscattered electrons SEM micrograph, Figure 2(b), that shows uniform grey contrast.

Table 1 shows the lattice parameter, the Yb occupancy factor in the 2a site and the ratio Yb_{2a}/Yb_{tot} in bulk and ribbon samples as a function of annealing time at 898 K. The bulk shows a progressive increase of the two parameters during annealing without levelling off at a constant value, suggesting that equilibrium is not reached even after 4 days of annealing, in agreement with literature data reporting that complete solubilisation of Yb is accomplished after at least 7 days of annealing at 1073 K [14, 16]. In the case of the ribbon, the values reported in table 1 drop after one day of annealing, subsequently increase reaching a plateau after 2-4 days of annealing, indicating attainment of the equilibrium. The larger amount of solubilized Yb in the as prepared ribbon is due to the quenching of the sample from a higher temperature where the Yb solubility is larger with respect to the annealing temperature [19]. The maximum amount of Yb solubilized in the skutterudite (around 0.19 for the ribbon annealed for 4 days) is lower than the stoichiometry (i.e. 0.25), indicating that about 25 % of Yb was lost during processing, in agreement with the results of EDX analysis.

The filling of the skutterudite cage occurs faster in the ribbon than in the bulk, as a consequence of the presence of a finer microstructure. The apparent diffusion coefficient, D_{app}, is given by [35]

$$D_{app} = D_l + D_b \frac{\delta}{d} \qquad (5)$$

where D_l is the lattice diffusion coefficient, D_b is the grain boundary diffusion coefficient, δ is the grain boundary width and d is the grain size. In the case of the rapidly solidified ribbon, the grain size is around 0.1 μm, while for the bulk, grain size is of the order of several tenths of microns. Thus, considering a constant value of the grain boundary width, the value of the δ/d ratio for the rapidly solidified ribbons is about two/three orders of magnitude larger than in the bulk, increasing the contribution of the grain boundary diffusion and the apparent diffusion coefficient in the ribbons.

As a consequence, the filling of the skutterudite cell with Yb atoms during annealing occurs faster in the ribbon than in the bulk, confirming that rapid solidification can be used as an intermediate step to reduce the total processing time.

The XRD patterns of the sintered samples show exclusively the crystallographic reflections belonging to $CoSb_3$, as shown in Figure 1(e) for ODP2 that was taken as a representative case.

However, SEM backscattered electron micrographs, Figures 2(d-f), reveal the presence of residual unreacted phases that are progressively less evident in ODP3 (CoSb, $CoSb_2$, Sb, $YbSb_2$), Figure 2(f), ODP1 ($CoSb_2$, $YbSb_2$), Figure 2 (d), and ODP2 ($CoSb_2$, Sb, $YbSb_2$), Figure 2 (e). In the case of ODP3, sintering of the starting multiphase powder (powder 3) promoted the homogenization of the sample forming an almost single phase dense massive material where some unreacted phases are still present, as shown in Figures 2(f). Table 2 shows the values of the lattice constant and the Yb occupancy factor in 2a site for the sintered samples. In the case of ODP1 and ODP2, the values obtained after sintering are slightly lower than those of the starting powders (powder 1 and powder 2), Table 1, because the data refer to different batches. However, the ratio between Yb_{2a}(ribbon)/Yb_{2a}(bulk) (about 1.30) is maintained in the corresponding ODP samples. The amount of Yb dissolved in the skutterudite is not expected to be affected by the sintering process because this was performed at a temperature lower than the annealing of the starting materials. The value of Yb occupancy factor in ODP2 is very close to the maximum solubility at 900 K (0.19) reported in Ref. [19], indicating that the system is almost at the equilibrium. In fact, only small traces of unreacted phase ($CoSb_2$, Sb, $YbSb_2$) are still present after sintering, as shown in Figure 2(e). In the case of ODP1, Figure 2(d), the amount of secondary phases is larger than in ODP2, as a consequence of the slower diffusivity in the bulk. The presence of secondary phases different from those predicted by the phase diagram [19], indicates that phase equilibrium as well as equilibrium Yb solubility were not attained in ODP1.

A similar consideration can be made for ODP3 where non equilibrium secondary phases are also present, Figure 2(f). In addition, the lower values of lattice constant and Yb occupancy factor with respect to ODP1 and ODP2 can be further explained by the lower solubility of Yb in the skutterudite at the temperature at which the sintering was performed [19].

The sintered samples show different values of relative density, as reported in Table 2. The significantly lower density of sample ODP1 (75 %) with respect to ODP2 (95 %) and ODP3 (90 %) can be explained by the different particles size distributions of the corresponding starting powders, estimated by SEM image analysis, that are reported in Figure 3. In fact, a multimodal distribution of the particles size, here represented by the broader peak (ODP2 and ODP3), allows a better packing of the powders before the sintering process. The slightly larger value of relative density of ODP2 (95 %) with respect to ODP3 (90 %) is probably due to the slower cooling rate of the sample, that reduced the effect of internal stresses induced by the different thermal contractions of the metallic sheath and the thermoelectric sintered powders. Conversely ODP3, experiencing a faster cooling, suffered a compressing action at low temperature inducing a loss in compaction of the grown grains, inducing a residual micro-porosity in the bulk.

Thermoelectric properties were measured only on ODP2 and ODP3 because ODP1 shows a value of relative density too low (75 %). ODP2 and ODP3 show similar values of the Seebeck coefficient as a function of temperature, Figure 4(a), indicating an n-type behaviour and suggesting that the presence of secondary phases in ODP3 and the different levels of filling with Yb between the two samples is too small to significantly affect the thermopower. As recently reported in Ref. [36], secondary phases affect thermoelectric properties of Yb-filled Co_4Sb_{12} skutterudites when they exceed a critical value (i.e. around 8 wt.%). Both ODP2 and ODP3 show decreasing values of the electrical conductivity, σ, as a function of temperature, revealing a behaviour typical of heavily doped semiconductors, Figure 4(b). This can be explained by the increased carrier concentration due to the filling with Yb [16, 21, 24]. However, ODP2 shows larger values of σ than ODP3. The effective electrical conductivity depends on the relative density of the sample and was calculated applying the Bruggeman symmetric model, where porosity is described as spherical inclusions [37, 38]. For relative densities of 90 % (ODP3) and 95 % (ODP2), the calculated effective electrical conductivities are 0.85 and 0.925 times the electrical conductivity of the fully dense material, respectively. The ratio between the calculated effective electrical conductivities of ODP3 and ODP2 is 0.92, while the ratio between the corresponding measured electrical conductivities is 0.89 at room temperature and 0.92 at 688 K. The agreement between the calculated and measured

values suggests that the different relative densities of ODP2 and ODP3 are responsible for the different measured electrical conductivities.

Figure 4(c) shows thermal diffusivity, α, as a function of temperature. Both samples show similar trends with a minimum around 600 K, however ODP2 shows lower values of α with respect to ODP3. Figure 4(d) shows the values of the specific heat at different temperature. Each point was obtained averaging four values obtained by means of the "height" and "area" methods on ODP2 and ODP3 samples. The error bars represent the standard deviation and the relative error is lower than 5 %, in agreement with the typical values for this technique. We can see that at room temperature the specific heat approaches the limit given by the Dulong-Petit approximation (C_p = 3R). To extend the temperature dependence of the specific heat across a wider range, the experimental data were fitted according the following typical expression [39]

$$C_p = 3R + aT + bT^2 \quad (6)$$

where R is the gas constant (8,314472 $Jmol^{-1}K^{-1}$), a and b are fitting parameters, which turn out equal to -3.13 10^{-3} K^{-1} and 9.15 10^{-6} K^{-2}, respectively.

From the data of thermal diffusivity, density and specific heat, the thermal conductivity was determined at different temperatures according to the relationship $\kappa = \alpha\rho C_p$, as shown in Figure 4(e). It can be seen that ODP2 and ODP3 show similar values between 300 K and 500 K, then above 500 K thermal conductivity of ODP2 becomes lower than the one of ODP3. The total thermal conductivity, κ, is given by $\kappa = \kappa_{el} + \kappa_{lat} + \kappa_{bp}$, where κ_{el}, κ_{lat} and κ_{bp} represent the electronic, lattice and bipolar contributions, respectively. The electronic contribution to the thermal conductivity, κ_{el}, was calculated through the Wiedemann-Franz law $\kappa_{el} = L\sigma T$, where L is the Lorentz constant ($2 \cdot 10^{-8}$ V^2K^{-2}), σ is the measured electrical conductivity and T is the absolute temperature. The bipolar contribution, κ_{bp}, is due to the thermal excitation of charge carriers (i.e. holes for n-type semiconductors) opposite to the dominant ones (i.e. electrons for n-type semiconductors) above a critical temperature [40].

In order to separate the contributions of κ_{lat} and κ_{bp}, we plotted the difference between κ and κ_{el} as a function of 1/T, as shown in the inset of Figure 2(e). The contribution of the bipolar thermal

conductivity [40], that is favoured at high temperature, becomes relevant when $(\kappa - \kappa_{el})$ vs. 1/T deviates from linearity (dotted lines are a guide to the eye), explaining the reason of the minimum in thermal conductivity, κ, observed around 600 K. ODP2 shows lower values of $(\kappa - \kappa_{el})$ than ODP3, because of the larger amount of Yb hosted in the skutterudite structure, that leads to an increase of phonon scattering and, consequently, to a reduction of lattice thermal conductivity In ODP2. The phonon scattering due to the larger Yb filling fraction compensates the increased electronic thermal conductivity caused by the larger density, leading to an overall lower thermal conductivity with respect to ODP3. Power factor was calculated from the measured values of the electrical conductivity and Seebeck coefficient as a function of temperature, as reported on the left hand side of Figure 4(f) (open and filled diamonds). The higher values shown by ODP2 with respect to ODP3 are due to the larger values of the electrical conductivity, related to higher density of the sample, since the two samples show the same values of the Seebeck coefficient. Finally, the figure of merit, ZT, as a function of temperature is reported on right hand side of Figure 4(f) (open and filled circles). ODP2 shows larger values of ZT with respect to ODP3 as a consequence of the larger power factor and the lower thermal conductivity. In the case of ODP2, ZT reaches a maximum value of 0.9 at 773 K, in agreement with the values reported in Refs. [16, 21] for similar values of Yb.

Figure 5 shows the thermoelectric properties (electrical conductivity, σ, Seebeck coefficient, S, lattice thermal conductivity, κ_{tot} - κ_{el}, and figure of merit, ZT) measured at 673 K as a function of the Yb content in Co_4Sb_{12}. The squares, diamond and triangles represent data from the literature (the reference is indicated by the corresponding number) while the stars are the data from this work. Data from the literature were grouped according to different symbols, depending on the technique used for determining the Yb content in the skutterudite phase. The data show some scattering likely due to presence of small amounts of secondary phases, different density of the samples, difference between nominal and actual Yb content. As a general trend, when the Yb content increases, electrical conductivity, σ, increases, while the absolute value of the Seebeck coefficient, |S|, decreases, as shown in Figure 5(a) and Figure 5(b), respectively. This trend is in agreement with the increased density of charge carrier due to the insertion of Yb atoms in the skutterudite

cage [16, 21, 24]. The actual Yb content in Co_4Sb_{12}, measured by XRD and EDX/EPMA (squares and diamonds, respectively), never exceeds 0.35, setting this value as the solubility limit [18, 19]. It was shown for $Fe_2Ni_2Sb_{12}$ (isoelectronic with Co_4Sb_{12}) that, as the Yb occupancy factor at 2a site in the skutterudite cage increases, the valence state of the Yb ion progressively decreases from trivalent to divalent, leading to the observed maximum solubility of the filler [9, 11]. This solubility limit was recently exceeded by using non equilibrium processing such as ball milling [36]. Since the samples obtained in Ref. [36] contained relevant amounts of secondary phases, that considerably affects thermoelectric properties, they were not taken in account in the present discussion. Considering the triangles, representing the thermoelectric property as a function of the nominal Yb content, we observe that, when $x < 0.35$, they follow the same trend of the squares and diamonds, while, when $x > 0.35$, they are shifted to the right with respect to the squares and diamonds, representing the thermoelectric property as a function of the actual Yb content. When the solubility limit of Yb is exceeded, the $YbSb_2$ secondary phase forms [18, 19] and its amount increases as the total Yb content increases. Thus, for $x > 0.35$, the triangles represent multiphase materials rather than single phase materials, and show an increasing metallic behaviour (i.e. increasing electrical conductivity, σ, and decreasing Seebeck coefficient, $|S|$) as the amount of secondary phase increases. The opposite effect of Yb filling on electrical conductivity and Seebeck coefficient leads to an optimized power factor, $S^2\sigma$, for $0.2<x<0.3$ (not shown). The effect of the Yb solubility limit is even more evident when the lattice thermal conductivity, taken as the difference between κ_{tot} and κ_{el}, is considered, Figure 5(c). In this case, the presence of a minimum of $\kappa_{tot} - \kappa_{el}$ around $x \cong 0.35$ indicates that phonon scattering is maximized in correspondence of the Yb solubility limit and that further addition of Yb is counterproductive. Finally, the combined effect of power factor and thermal conductivity leads to an optimized value of the figure of merit, ZT, for $0.20<x<0.25$, as shown in Figure 5(d).

Conclusions

In this work, we explored the effect of different processing routes on the structure, microstructure and thermoelectric properties of Yb-doped $CoSb_3$ compound. Uncontrolled cooling of the melt

leads to the formation of a porous bulk with coarse microstructure. Rapid solidification by planar flow casting allows the formation of fragmented ribbons with a refined microstructure and no porosity. In both cases, as prepared samples show multiple phases, thus annealing was needed to promote homogenization. The solubilisation of Yb in the skutterudite structure is significantly faster for the rapidly solidified ribbons as a consequence of the increased grain boundary diffusivity with respect to the bulk sample. Thus, rapid solidification reveals to be a convenient intermediate step to decrease the total processing time for the synthesis of filled skutterudites.

Powders obtained by grinding the bulk show a narrower particle size distribution with respect to the powders obtained from the ribbons, leading to a lower density in the sintered samples. Sintering of the powders obtained from as quenched and annealed ribbons leads to almost single phase dense samples, however Yb filling is higher when annealed ribbons are used.

Thermoelectric properties of the sintered samples depend on porosity and Yb filling. As expected, larger values of electrical conductivity were found in denser samples. Concerning thermal conductivity, the interplay between density and Yb filling is more complex. On the one hand, less dense samples are expected to show lower values of thermal conductivity. On the other hand, denser samples show a larger Yb filling that leads to a lower lattice thermal diffusivity and, overall, to a lower thermal conductivity with respect to less dense samples. A survey of literature data shows a direct correlation between thermoelectric properties and Yb content when the latter is below the solubility limit. When the Yb content exceeds the solubility limit, thermoelectric properties show a deviation from the observed trend due to the presence of secondary phases affecting thermoelectric behaviour.

Acknowledgements

A. Castellero, S. Branz and M. Baricco thank Fondazione CRT for financial support (grant n. 2015.1530)

References

[1] G.J. Snyder, E.S. Toberer, Complex thermoelectric materials, Nature Mater. 7 (2008) 105-114.

[2] B. Sales, D. Mandrus, B. Chakoumakos, V. Keppens, J. Thompson, Filled skutterudite antimonides: Electron crystals and phonon glasses, Phys. Rev. B 56 (1997) 15081-15089.

[3] B.C. Sales, D. Mandrus, R.K. Williams, Filled Skutterudite Antimonides: A New Class of Thermoelectric Materials, Science 272 (1996) 1325-1328.

[4] G.S. Nolas, M. Kaeser, R.T. Littleton IV, T.M. Tritt, High figure of merit in partially filled ytterbium skutterudite materials, Appl. Phys. Lett. 77 (2000) 1855-1857.

[5] L.D. Chen, T. Kawahara, X.F. Tang, T. Goto, T. Hirai, J.S. Dyck, W. Chen, C. Uher, Anomalous barium filling fraction and n-type thermoelectric performance of $Ba_yCo_4Sb_{12}$, J. Appl. Phys. 90 (2001) 1864-1868.

[6] M. Puyet, B. Lenoir, A. Dauscher, M. Dehmas, C. Stiewe, E. Müller, High temperature transport properties of partially filled $Ca_xCo_4Sb_{12}$ skutterudites, J. Appl. Phys. 95 (2004) 4852-4855.

[7] C. Uher, Skutterudite-based thermoelectric, in: D.M. Rowe (Ed), Thermoelectrics Handbook - Macro to Nano, Taylor and Francis, Boca Raton, 2006, chapter 34.

[8] B. Bourgoin, D. Bérardan, E. Alleno, C. Godart, O. Rouleau and E. Leroy, Preparation and thermopower of new mischmetal-based partially filles skutterudites $Mm_yFe_{4-x}(Co/Ni)_xSb_{12}$, J. Alloys Compd. 399 (2005) 47-51.

[9] D. Bérardan, E. Alleno, C. Godart, O. Rouleau and J. Rodriguez-Carvajal, Preparation and chemical properties of the skutterudites $(Ce\text{-}Yb)_yFe_{4-x}(Co/Ni)_xSb_{12}$, Mater. Res. Bull. 40 (2005) 537-551.

[10] C. Artini, G. Zanicchi, G.A. Costa, M.M. Carnasciali, C. Fanciulli and Riccardo Carlini, Correlations between Structural and Electronic Properties in the Filled Skutterudite $Sm_y(Fe_xNi_{1-x})_4Sb_{12}$, Inorg. Chem. 55 (2016) 2574- 2583.

[11] A. Kaltzoglou, P. Vaqueiro, K.S. Knight and A.V. Powell, Synthesis, characterization and physical properties of the skutterudites $Yb_xFe_2Ni_2Sb_{12}$, J. Solid State Chem. 193 (2012) 36-41.

[12] X. Y. Zhao, X. Shi, L. D. Chen, W. Q. Zhang, S. Q. Bai, Y. Z. Pei, X. Y. Li, T. Goto, Synthesis of $Yb_yCo_4Sb_{12}/Yb_2O_3$ composites and their thermoelectric properties, Appl. Phys. Lett. 89 (2006) 092121.

[13] Z. Yao, X.Y. Li, Y.S. Tang, L.D. Chen, Genomic Effects of the Quenching Process on the Microstructure and Thermoelectric Properties of $Yb_{0.3}Co_4Sb_{12}$, J. Electron. Mater. 44 (2015) 1890-1895.

[14] Z. Xiong, X. Chen, X. Huang, S. Bai, L. Chen, High thermoelectric performance of $Yb_{0.26}Co_4Sb_{12}$/yGaSb nanocomposites originating from scattering electrons of low energy, Acta Mater. 58 (2010) 3995-4002.

[15] H. Li, X. Tang, X. Su, Q. Zhang, C. Uher, Nanostructured bulk $Yb_xCo_4Sb_{12}$ with high thermoelectric performance prepared by the rapid solidification method, J. Phys. D: Appl. Phys. 42 (2009) 145409.

[16] J.R. Salvador , J. Yang , X. Shi , H. Wang , A.A. Wereszczak , H. Kong, C. Uher, Transport and mechanical properties of Yb-filled Skutterudites, Phil. Mag. 89 (2009) 1517–1534.

[17] X. Shi, H. Kong, C.-P. Li, C. Uher, J. Yang, J. R. Salvador, H. Wang, L. Chen, W. Zhang, Low thermal conductivity and high thermoelectric figure of merit in n-type $Ba_xYb_yCo_4Sb_{12}$ double-filled skutterudites, Appl. Phys. Lett. 92 (2008) 182101.

[18] S. Wang, J.R. Salvador, J. Yang, P. Wei, B. Duan, J. Yang, High-performance n-type $Yb_xCo_4Sb_{12}$: from partially filled skutterudites towards composite thermoelectrics, NPG Asia Mater. 8 (2016) e285.

[19] Y. Tang, S.-W. Chen, G.J. Snyder, Temperature dependent solubility of Yb in Yb-$CoSb_3$ skutterudite and its effect on preparation, optimization and lifetime of thermoelectrics, J. Materiomics 1 (2015) 75-84.

[20] H. Liu, X. Zhao, T. Zhu, Y. Gu, Thermoelectric properties of $Yb_xCo_4Sb_{12}$ system, J. Rare Earths 30 (2012) 456-459.

[21] K.-H. Park, W.-S. Seo, D.-K. Shin, I.-H. Kim, Thermoelectric properties of Yb-filled CoSb3 skutterudites, J. Korean Phys. Soc. 65 (2014) 491-495.

[22] H.Y. Geng, S. Ochi, J.Q. Guo, Solidification contraction-free synthesis for the $Yb_{0.15}Co_4Sb_{12}$ bulk material, Appl. Phys. Lett. 91 (2007) 022106.

[23] T. Dahal, Q. Jie, G. Joshi, S. Chen, C. Guo, Y. Lan, Z. Ren, Thermoelectric property enhancement in Yb-doped n-type skutterudites $Yb_xCo_4Sb_{12}$, Acta Materialia 75 (2014) 316-321.

[24] J. Yang Q. Hao, H. Wang, Y.C. Lan, Q.Y. He, A. Minnich, D.Z. Wang, J.A. Harriman, V.M. Varki, M.S. Dresselhaus, G. Chen, Z.F. Ren, Solubility study of Yb in n-type skutterudites $Yb_xCo_4Sb_{12}$ and their enhanced thermoelectric properties, Phys. Rev. B 80 (2009) 115329.

[25] H. Okamoto, Phase diagrams for binary alloys, ASM International, Materials Park (OH), 2000, p. 258.

[26] B. Alinejad, A. Castellero, M. Baricco, Full dense $CoSb_3$ single phase with high thermoelectric performance prepared by oscillated cooling method, Scripta Materialia 113 (2016) 110-113.

[27] C. Artini, A. Castellero, M. Baricco, M.T. Buscaglia, R. Carlini, Structure, microstructure and microhardness of rapidly solidified $Sm_y(Fe_xNi_{1-x})_4Sb_{12}$ (x = 0.45, 0.50, 0.70, 1) thermoelectric compounds, Solid State Sciences 79 (2018) 71-78.

[28] M. Baricco, E. Bosco, E. Olivetti, M. Palumbo, P. Rizzi, A. Stantero, L. Battezzati, Rapid solidification of alloys, Int. J. Mater. Prod. Technol. 20 (2004) 358-376.

[29] M. Baricco, A. Castellero, M. Di Chio, Zs. Kovacs, P. Rizzi, M. Satta and A. Ziggiotti, "Thermal stability and hardness of Mg–Cu–Au–Y amorphous alloys", J. Alloys Compd.,434–435 (2007) 183-186.

[30] S.K. Bux, J.-P. Fleurial and R.B. Kaner, Nanostructured materials for thermoelectric applications, Chem. Commun. 46 (2010) 8311–8324.

[31] S. Ceresara, C. Fanciulli, F. Passaretti, D. Vasilevskiy, Texturing of $(Bi_{0.2}Sb_{0.8})_2Te_3$ Nanopowders by Open Die Pressing, J. Electron. Mater. 42 (2013) 1529-1534.

[32] http://maud.radiographema.com

[33] S. Boldrini, A. Famengo, F. Montagner, S. Battiston, S.Fiameni, M. Fabrizio and S. Barison, Test rig for high-temperature thermopower and electrical conductivity measurements, J. Electron. Mater. 42(2013) 1319-1323.

[34] R.F. Speyer, Thermal analysis of materials, Marcel Dekker Inc., New York, 1994, pp. 79-80.

[35] D.A. Porter, K.E. Easterling, Phase Transformations in Metals and Alloys, 2nd edition, Chapmann & Hall, London, 1992, p. 101.

[36] B. Ryll, A. Schmitz, J. de Boor, A. Franz, P.S. Whitfield, M. Reehuis, A. Hoser, E. Müller, K. Habicht and K. Fritsch, Structure, Phase Composition, and Thermoelectric Properties of $Yb_xCo_4Sb_{12}$ and Their Dependence on Synthesis Method, Appl. Energy Mater. 1 (2018) 113-122.

[37] D.A.G. Bruggeman, The calculation of various physical constants of heterogeneous substances: I. The dielectric constants and conductivities of mixtures composed of isotropic substances. Ann. Phys., 24 (1935) 636-664.

[38] J.M.V.A. Koelman, A. de Kuijper, An effective medium model for the electric conductivity of an N-component anisotropic and percolating mixture, Physica A,247 (1997) 10-22.

[39] A.T. Dinsdale, SGTE data for pure elements, CALPHAD 15 (1991) 317-425.

[40] S. Wang, J. Yang, T. Toll, J. Yang, W. Zhang, X. Tang, Conductivity-limiting bipolar thermal conductivity in semiconductors, Sci. Rep. 5 (2015) 10136.

Tables captions

Table 1. Lattice parameter, a, Yb occupancy factor in the 2a site, Yb_{2a}, ratio (Yb_{2a}/Yb_{tot}) between Yb in the skutterudite cage, Yb_{2a}, and total amount of Yb, Yb_{tot}, Co/Sb ratio as a function of the annealing time at 898 K ($Yb_{skutterudite}$). Lattice parameter and Yb_{2a} occupancy factor were determined by Rietveld refinement of the XRD patterns of Figure 1, the Co/Sb ratio was determined by EDX analysis.

Table 2. Lattice parameter, Yb_{2a} occupancy factor, relative density and Co/Sb ratio of the as sintered ODP1, ODP2 and ODP3 samples.

Table 1

Annealing time (days)	Bulk				Ribbon			
	a (Å)	**Yb_{2a}**	**Yb_{2a}/Yb_{tot}**	**Co/Sb**	**a (Å)**	**Yb_{2a}**	**Yb_{2a}/Yb_{tot}**	**Co/Sb**
0	9.0459	0.12(2)	0.76	3.40	9.0530	0.19(2)	0.98	3.30
1	9.0458	0.12(1)	0.75		9.0482	0.14(2)	0.72	
2	9.0471	0.12(9)	0.80		9.0522	0.18(4)	0.93	
4	9.0486	0.14(4)	0.90		9.0527	0.18(8)	0.98	

Table 2

Sample	Lattice parameter (Å)	Yb_{2a} occupancy factor	Relative density (%)	Sb/Co
ODP1	9.0478	0.13(6)	75	3.40
ODP2	9.0512	0.17(6)	95	3.24
ODP3	9.0462	0.12(6)	90	3.35

Figures captions

Figure 1. X-ray diffraction (XRD) patterns. (a) as prepared bulk ingots. (b) annealed (4 days at 898 K) bulk ingots. (c) as prepared rapidly solidified (RS) ribbons. (d) annealed (4 days at 898 K) rapidly solidified (RS) ribbons. (e) ODP2 sintered sample. Black points, red curves and green curves represent experimental data, refined patterns and differences between experimental and refined patterns, respectively.

Figure 2. Backscattered electron SEM images. (a) annealed (4 days at 898 K) bulk ingot. (b) annealed (4 days at 898 K) rapidly solidified (RS) ribbon. (c) as prepared rapidly solidified (RS) ribbon. (d), (e) and (f) sintered ODP1, ODP2 and ODP3 samples, respectively.

Figure 3. Particle size distribution for powder 1, obtained by grinding the annealed bulk ingot, powder 2 and powder 3, obtained by grinding annealed and as quenched rapidly solidified ribbons, respectively.

Figure 4. Thermoelectric and thermophysical properties of sintered ODP2 (open symbols) and ODP3 (filled symbols) samples as a function of temperature. (a) Seebeck coefficient, S. (b) Electrical conductivity, σ. (c) Thermal diffusivity, α. (d) Averaged experimental values of the specific heat, C_p, measured on ODP2 and ODP3 samples (black squares) with the corresponding fitting curve (continuous line); on the basis of the fitting result, specific heat is extrapolated in a larger temperature range (dashed line). (e) Thermal conductivity, κ; κ_{tot} and κ_{el} represent the total and electronic thermal conductivities, respectively; the inset shows the difference between κ_{tot} and κ_{el} as a function of the inverse of temperature: the deviation from linearity at high temperature indicates the onset for bipolar conduction. (f) Left hand side (diamonds): power factor, $S^2\sigma$. Right hand side (circles): figure of merit, ZT.

Figure 5. Thermoelectric properties at 673 K as a function of the Yb content in the Co_4Sb_{12} cell. (a) electrical conductivity, σ. (b) Seebeck coefficient, S. (c) lattice thermal conductivity, assessed as κ_{tot}-κ_{el}. (d) figure of merit, ZT. The squares, diamonds and triangles represent data literature (the numbers indicate the corresponding references), while the stars represent data from this work. The legend for the different symbols indicates the method how the actual Yb content was determined (XRD, EDS/EPMA, nominal composition).

Figure 1

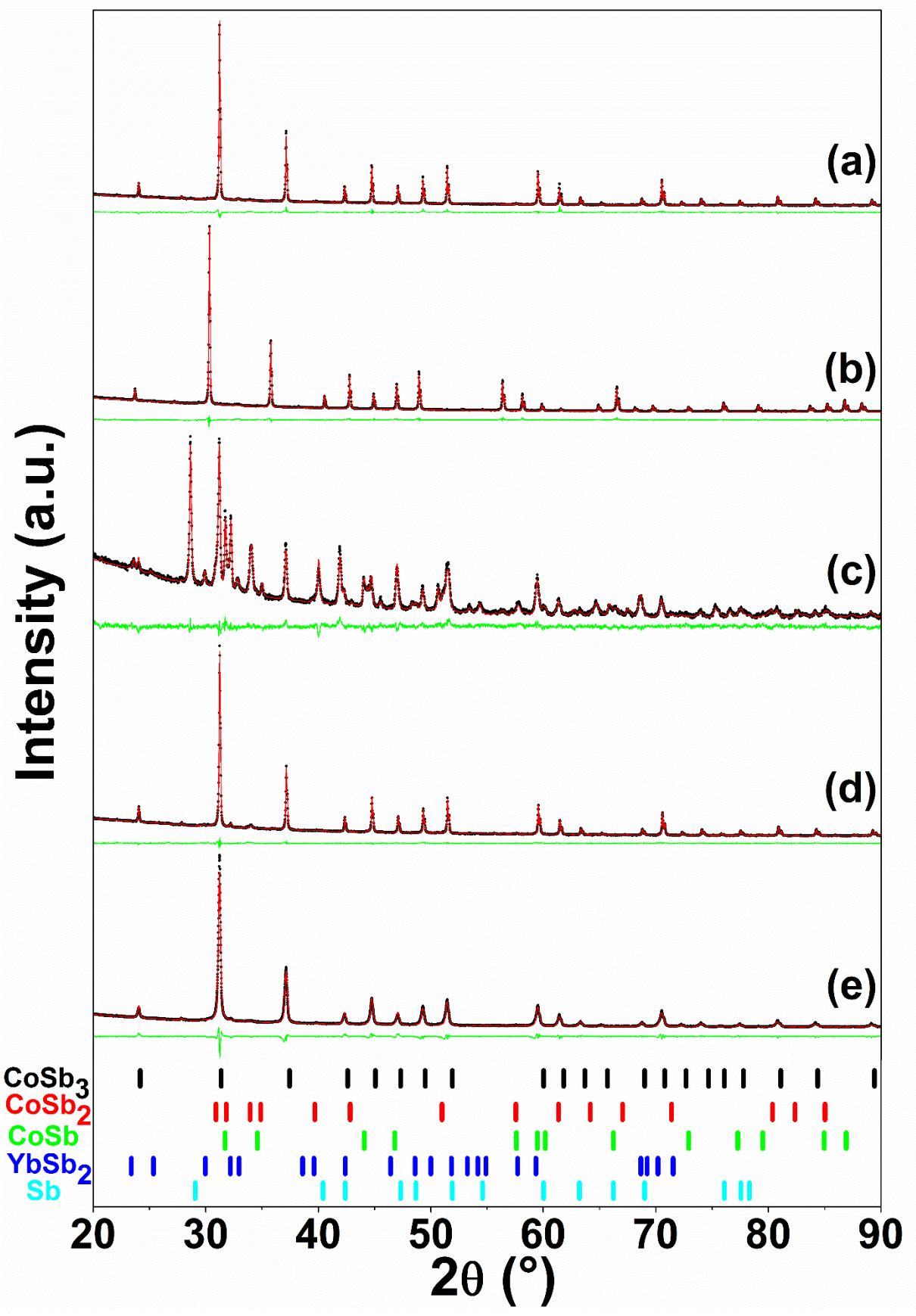
(a)
(b)
(c)
(d)
(e)
Intensity (a.u.)
CoSb3
CoSb2
CoSb
YbSb2
Sb
20
30
40
50
60
70
80
90
2θ (°)

Figure 2

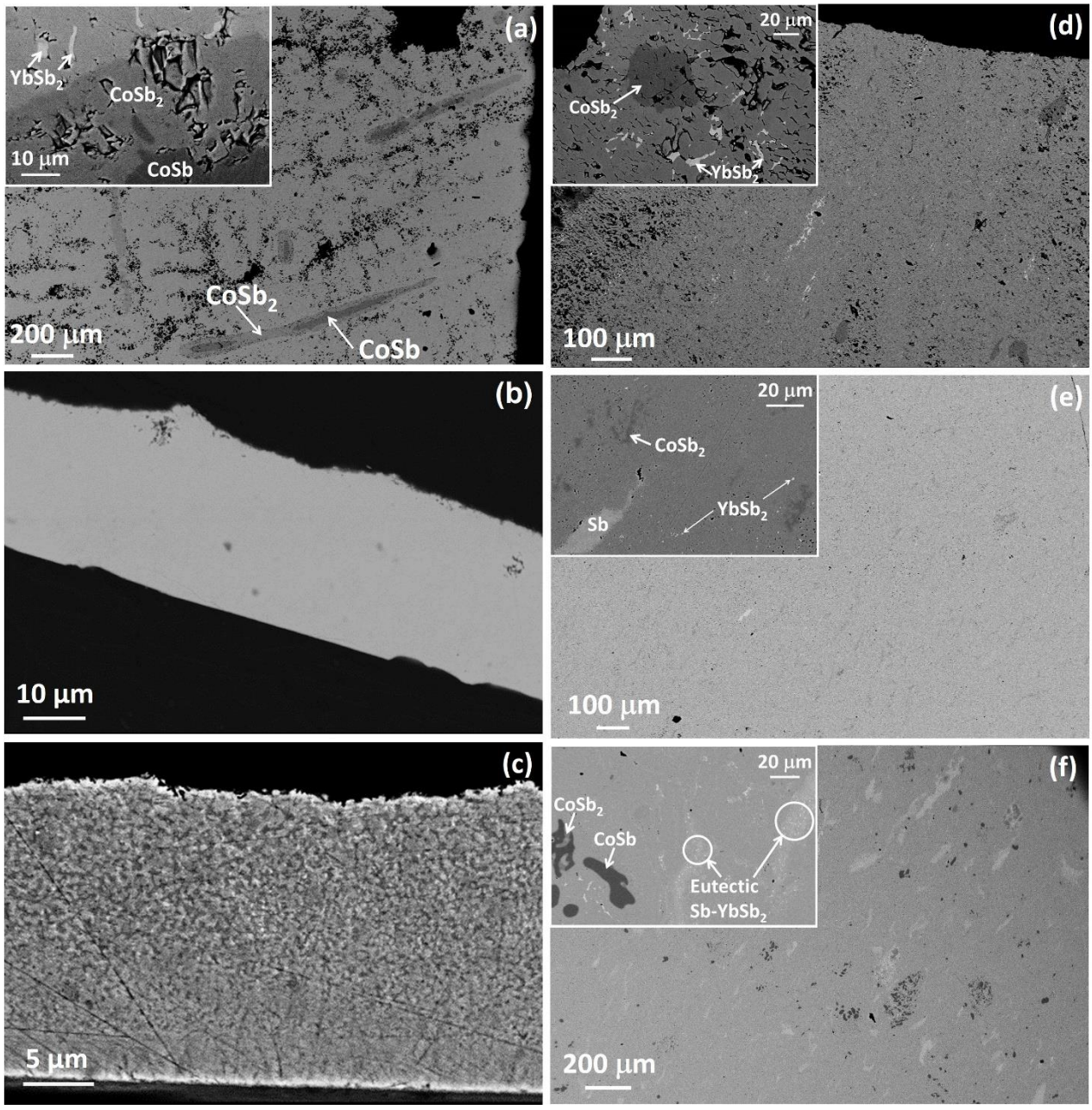
(a)
YbSb2
CoSb2
10 μm
CoSb
CoSb2
200 μm
CoSb
(b)
10 μm
(c)
5 μm
(d)
20 μm
CoSb2
YbSb2
100 μm
(e)
20 μm
CoSb2
Sb
YbSb2
100 μm
(f)
20 μm
CoSb2
CoSb
Eutectic
Sb-YbSb2
200 μm

Figure 3

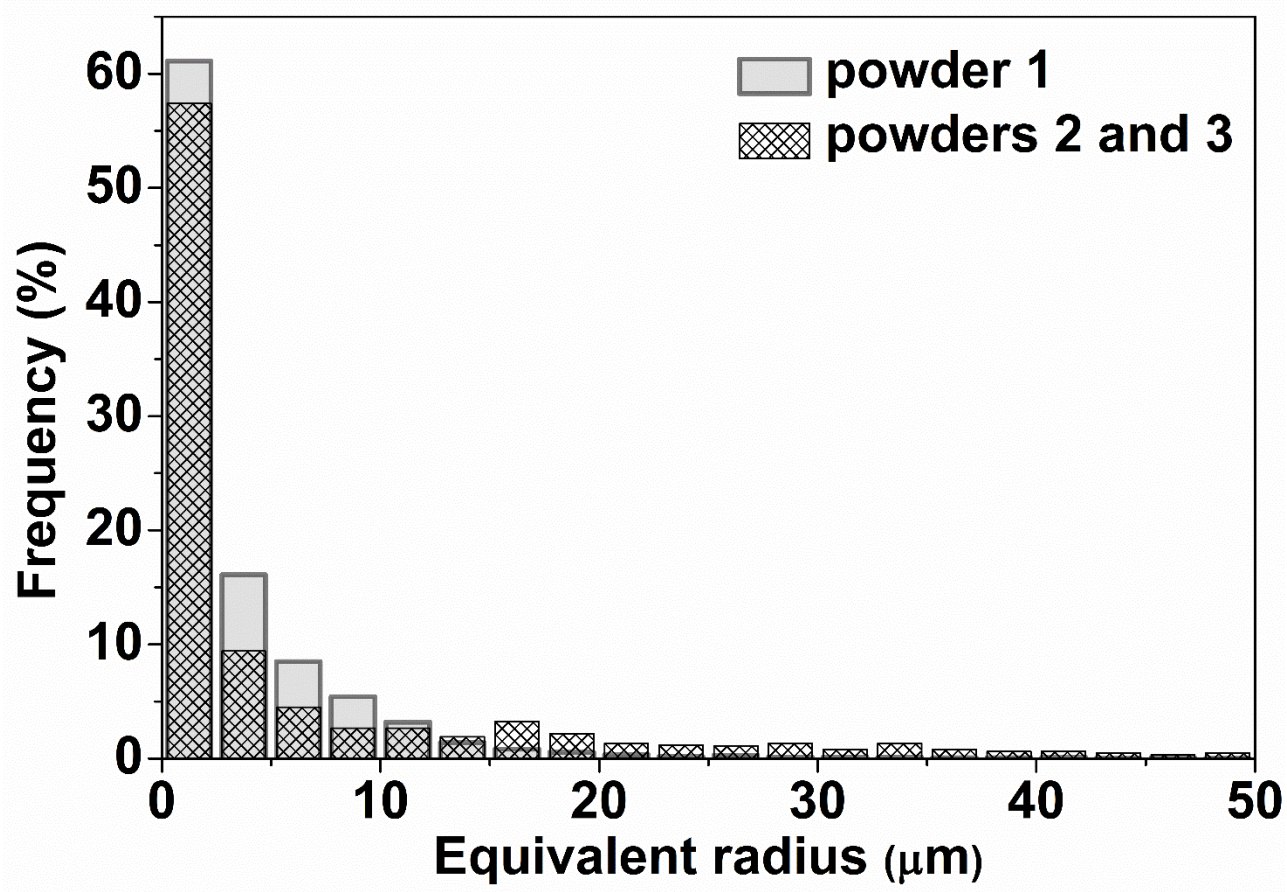
powder 1
powders 2 and 3
Frequency (%)
0
10
20
30
40
50
60
0
10
20
30
40
50
Equivalent radius (μm)

Figure 4

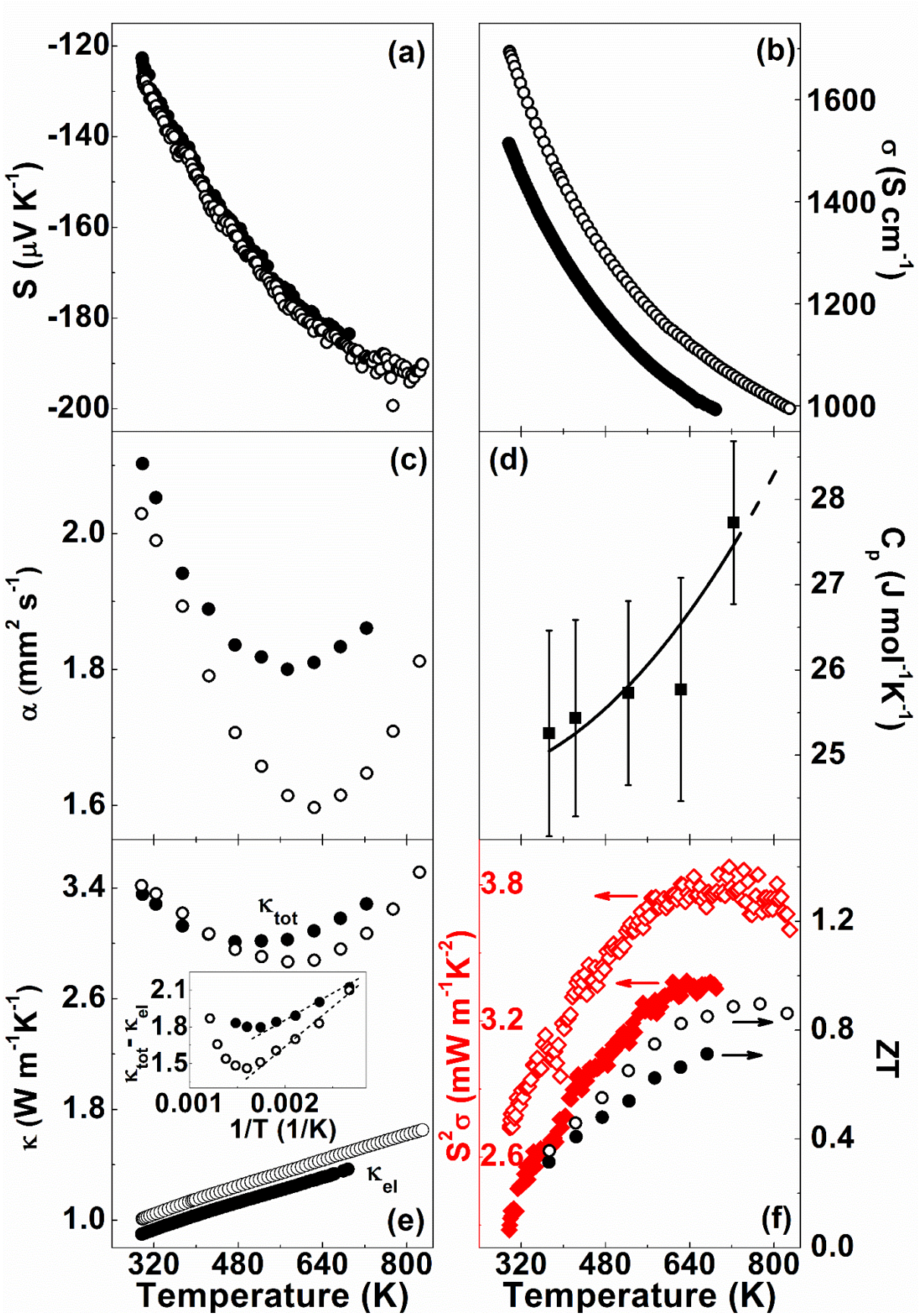
(a)
(b)
(c)
(d)
(e)
(f)
S (μV K-1)
σ (S cm-1)
α (mm2 s-1)
Cp (J mol-1K-1)
κ (W m-1K-1)
S2σ (mW m-1K-2)
ZT
κtot
κel
κtot - κel
1/T (1/K)
Temperature (K)
Temperature (K)

Figure 5

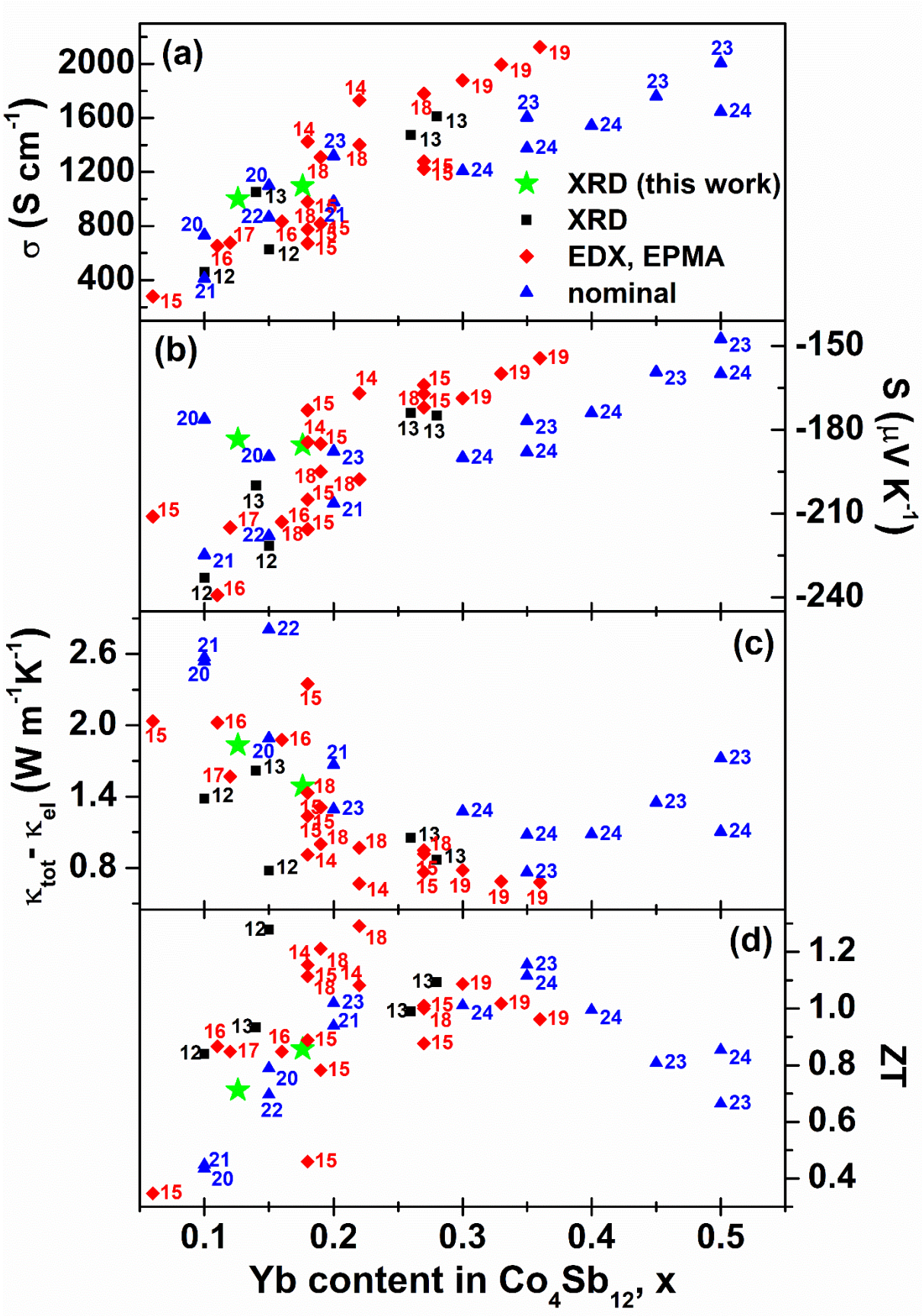
(a)
(b)
(c)
(d)
σ (S cm-1)
S (μV K-1)
κtot - κel (W m-1K-1)
ZT
Yb content in Co4Sb12, x
XRD (this work)
XRD
EDX, EPMA
nominal